

# NJC

Accepted Manuscript



This is an *Accepted Manuscript*, which has been through the Royal Society of Chemistry peer review process and has been accepted for publication.

*Accepted Manuscripts* are published online shortly after acceptance, before technical editing, formatting and proof reading. Using this free service, authors can make their results available to the community, in citable form, before we publish the edited article. We will replace this *Accepted Manuscript* with the edited and formatted *Advance Article* as soon as it is available.

You can find more information about *Accepted Manuscripts* in the [Information for Authors](#).

Please note that technical editing may introduce minor changes to the text and/or graphics, which may alter content. The journal's standard [Terms & Conditions](#) and the [Ethical guidelines](#) still apply. In no event shall the Royal Society of Chemistry be held responsible for any errors or omissions in this *Accepted Manuscript* or any consequences arising from the use of any information it contains.

## Synthesis and DFT studies of an antitumor active spiro-oxindole

Adel S. Girgis,\*<sup>a</sup> Ahmed F. Mabied,<sup>b</sup> Jacek Stawinski,<sup>c</sup> Lamees Hegazy,<sup>d</sup> Riham F. George,<sup>e</sup> Hanaa Farag,<sup>a</sup> ElSayed M. Shalaby<sup>b</sup> and I. S. Ahmed Farag<sup>b</sup>

<sup>a</sup> Pesticide Chemistry Department, National Research Centre, Dokki, Giza 12622, Egypt.

<sup>b</sup> X-Ray Crystallography Lab., Physics Division, National Research Centre, Dokki, Giza 12622, Egypt.

<sup>c</sup> Department of Organic Chemistry, Arrhenius Laboratory, Stockholm University, S-10691 Stockholm, Sweden.

<sup>d</sup> BioDiscovery group, Agra 282001, India.

<sup>e</sup> Pharmaceutical Chemistry Department, Faculty of Pharmacy, Cairo University, Cairo, Egypt.

\*Corresponding authors E-mail: [girgisas10@yahoo.com](mailto:girgisas10@yahoo.com); Fax: +33370931; Tel: 01220447199.

### Abstract

An anti-oncological active spiro-oxindole **7** was synthesized regioselectively *via* [3+2]-cycloaddition reaction of azomethine ylide to exocyclic olefinic linkage of 4-piperidone **6**, exhibiting properties against diverse tumor cell lines including leukemia, melanoma and cancers of the lung, colon, brain, ovary, breast, prostate, and kidney. Compound **7** crystallizes in the monoclinic system and P21/c space group with four molecules in the unit cell. The structure was also studied by AM1, PM3 and DFT techniques. DFT studies support the reaction's stereochemical selectivity and determine the molecular electrostatic potential and frontier molecular orbitals.

### Keywords:

Piperidone, Spiro-oxindole, X-ray, DFT, AM1, PM3, Antitumor.

### Introduction

Despite significant advances in the diagnostic and therapeutic techniques, cancer is now the second most frequent cause of death after circulatory diseases. The worldwide cancer burden is expected to increase by as much as 15 million new cancer cases per year by 2020, according to the World Health Organization, unless further preventive measures are put into practice.<sup>1,2</sup> Cancer is a class of multigenic disease characterized by a diversity of genetic and epigenetic alterations and can be cured by preventing the rapid proliferation of cancer cells for which the replication of DNA is to be arrested.<sup>3</sup> Generally, cancers of the breast, lung, colorectal, and prostate are the most frequent types in developed countries while those of the stomach, liver, oral cavity, and cervix, in developing countries, although this pattern seems to be evolving, especially due to population aging and life style changes.<sup>4,5</sup> Chemotherapy is still one of the primary modalities for the treatment of cancer, however, the use of available chemotherapeutics is often limited mainly due to toxicities and emerging drug resistance.<sup>6</sup>

The present study deals with the synthesis of a novel spiropyrrolidine-oxindole derivative. The interest in this class of compounds is attributed to the kinase inhibitory properties of 2-oxindoles.<sup>7-11</sup> Additionally, this framework forms the core structure of many alkaloids and natural products exhibiting potent biological/pharmacological properties. For example, mitraphylline **1**, isolated from *Uncaria tomentosa*, possesses potent antitumor properties against human brain cancer cell lines, neuroblastoma SKN-BE(2) and malignant glioma GAMG,<sup>12</sup> while spirotryprostatins A (**2**) and B (**3**) (isolated from the fermentation broth of *Aspergillus fumigatus*) are powerful inhibitors of the G2/M progression cell division in mammalian tsFT210 cells<sup>13,14</sup> (Figure 1).

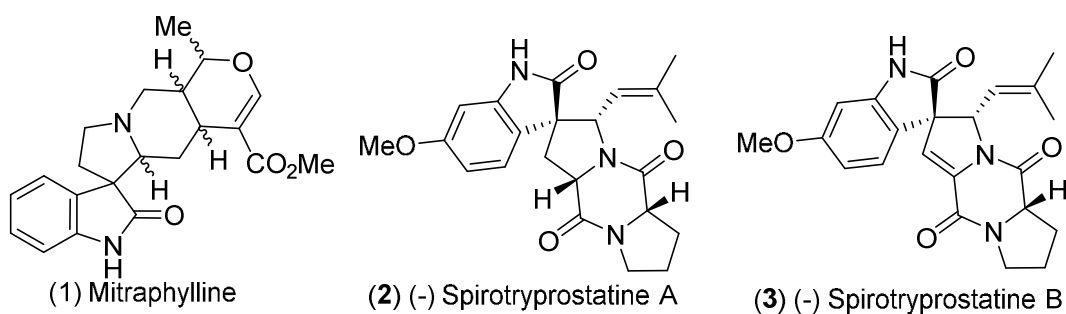


**Figure 1.** Natural pharmacological active 2-oxindole containing-compounds.

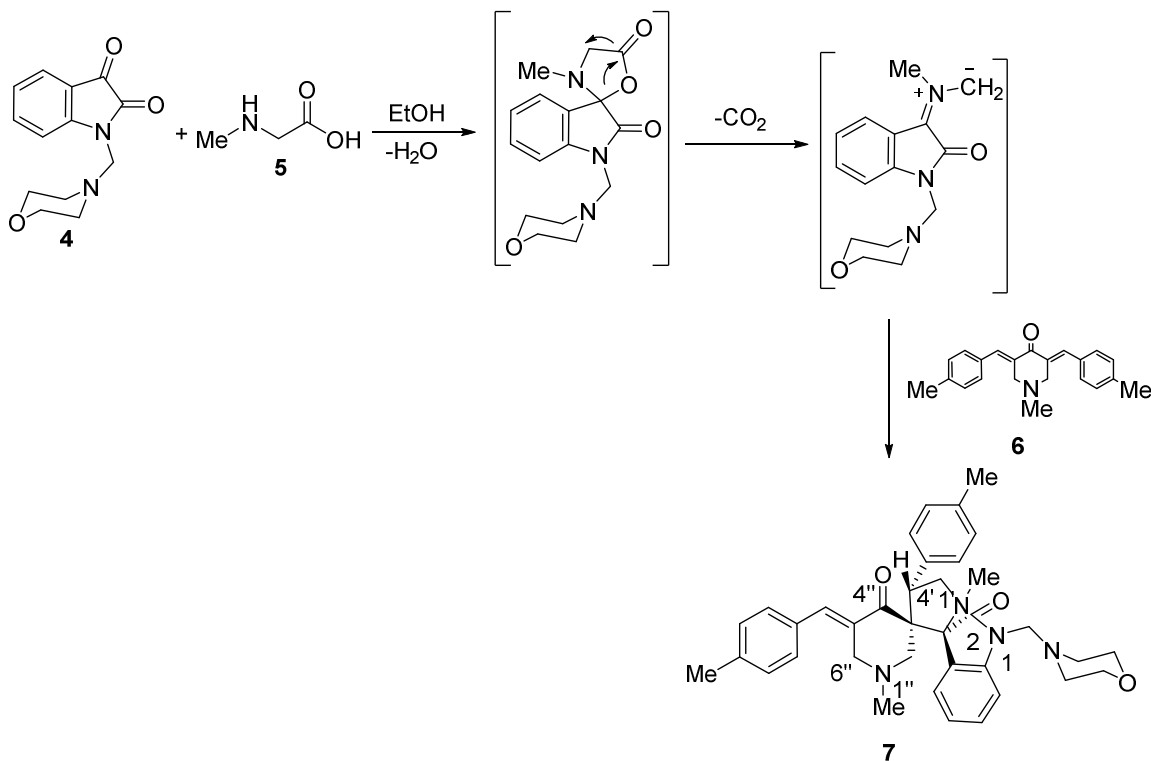
Encouraged by these literature reports and our previous successful research in this area,<sup>15-22</sup> we decided to explore further therapeutic potential of this class of compounds by designing new spiropyrrolidine-oxindole **7** (Scheme 1) as potential anticancer agent. This paper describes a stereoselective synthesis of spiropyrrolidine-oxindole **7**, its chemical characterization and antitumor properties against diverse tumor cell lines. To get a deeper insight into structural feature of the synthesized compound **7**, these results were appended with X-ray analysis and computational studies. Single crystal X-ray studies that have capacity to identify the enantiomers and/or diastereomers of chiral molecules,<sup>23</sup> were used in this work to delineate stereochemical features of **7**, difficult to obtain by spectral methods. These experimental data were complemented by results from different computational chemistry techniques (MM<sup>+</sup>, AM1, PM3, and DFT) that permitted comparison of the experimental versus theoretical data. Also studies on molecular electrostatic potential (MEP) and frontier molecular orbitals (FMO) of compound **7**, that can be of importance for quantitative structure activity relationships (QSAR) and 3D-pharmacophore modelling, were carried out.

## Results and discussion

### Chemistry

1,3-Dipolar cycloaddition reaction of non-stabilized azomethine ylide, (generated *in situ* via decarboxylative condensation of 1-[(4-morpholinyl)methylene]-1*H*-indole-2,3-dione **4** with sarcosine **5**) and 3*E*,5*E*-bis[(4-methylphenyl)methylidene]-1-methyl-4-piperidone **6** in refluxing ethanol proceeded regioselectively affording a single product as monitored by TLC. The structure of the isolated, colorless compound was assigned as 1',1''-dimethyl-4'-(4-methylphenyl)-5''-[(4-methylphenyl)methylidene]-1-[(4-morpholinyl)methylene]-dispiro[3*H*-indole-3,2'-pyrrolidine-3',3''-piperidine]-2(1*H*),4''-dione **7** based on the spectroscopic (IR, <sup>1</sup>H-, <sup>13</sup>C-NMR, <sup>1</sup>H,<sup>1</sup>H-COSY, HSQC) and elemental analysis data. The reaction commences with a nucleophilic attack of the amino group of sarcosine **5** on the 3-carbonyl function of 1-[(4-morpholinyl)methylene]-1*H*-indole-2,3-dione **4**, followed by dehydration to form a spiro-oxazolidinone system. This expels carbon dioxide to generate a reactive, non-stabilized azomethine ylide, that undergoes *in situ* 1,3-dipolar cycloaddition with the exocyclic olefinic linkage of 3,5-

bis[(4-methylphenyl)methylidene]-1-methyl-4-piperidone **6** eventually affording **7** (Scheme 1).



**Scheme 1** A synthetic route towards spiropyrrolidine-oxindole **7**.

The IR spectrum of **7** (Figure S1 of the supplementary material) shows a strong stretching vibration bands at  $\nu = 1703, 1686 \text{ cm}^{-1}$  assignable for the ketonic and amidic carbonyl functions, respectively. The <sup>1</sup>H-NMR spectrum of **7** (Figure S2 of the supplementary material) reveals the methylene protons *H*<sub>2</sub>C-5', *H*<sub>2</sub>C-2'' and *H*<sub>2</sub>C-6'' as diastereotopic two spin systems, and the methine *HC*-4' appears as a double doublet signal at  $\delta_{\text{H}} = 4.78 \text{ ppm}$  due to the mutual coupling with the diastereotopic pyrrolidinyl *H*<sub>2</sub>C-5'. The methylene protons attached to the indolyl *N*-1 also appear as diastereotopic protons (two doublets at  $\delta_{\text{H}} = 4.07$  and  $4.50 \text{ ppm}$ ). The morpholinyl methylene protons give two triplet at  $\delta_{\text{H}} = 2.54$  and  $3.62 \text{ ppm}$ . <sup>1</sup>H,<sup>1</sup>H-COSY spectrum of compound **7** (Figure S3 of the supplementary material) supports these interpretations. The <sup>13</sup>C-NMR spectrum of **7** (Figure S4 of supplementary material) exhibits the methylene carbon *H*<sub>2</sub>C-6'' at  $\delta_{\text{c}} = 56.7 \text{ ppm}$ . The methylene carbons of the piperidine *H*<sub>2</sub>C-2'' and pyrrolidine

$H_2C-5'$  are overlapped at  $\delta_c = 57.3$  ppm. The pyrrolidine  $HC-4'$  carbon resonates at  $\delta_c = 45.1$  and the methyl groups attached to the pyrrolidine  $N-1'$  and piperidine  $N-1''$  show signals at  $\delta_c = 35.0$  and  $45.0$ , respectively. The methyl carbons of tolyl groups appear at  $\delta_c = 21.1$  and  $21.4$  ppm. The morpholinyl methylene carbons resonate at  $\delta_c = 51.2$  and  $66.8$  ppm, the spiro-carbons  $C-3'$  ( $C-3''$ ) and  $C-3$  ( $C-2'$ ) at  $\delta_c = 66.3$  and  $75.5$  ppm, respectively, and the carbonyl carbons  $C-2$  and  $C-4''$ , at  $\delta_c = 176.4$  and  $198.4$  ppm, respectively (*c.f.* experimental section).  $^1H, ^{13}C$ -heteronuclear single quantum coherence (HSQC) spectrum of compound **7** supports these assignments (Figures S5 of the supplementary material).

### Single crystal X-ray studies

Spiropyrrolidine-oxindole **7** crystallizes in the monoclinic system and P21/c space group with four molecules in the unit cell. The asymmetric unit in the structure contains only one molecule. Figure 2 shows an ORTEP view of compound **7**. Two spiro centers are at C17, where the piperidine and pyrrolidine rings are connected, and at C12, where the pyrrolidine and indole rings are attached. In general, the values of bond lengths and angles (Tables S1, S2 of supplementary material) are in the range typical for this class of compounds which structures have been determined previously.<sup>17,19,24-28</sup>

The X-ray structure identifies the most important stereochemical features of spiropyrrolidine-oxindole **7**, i.e. *E*-configuration of the olefinic bond between C29 and C30, and stereochemistry of the pyrrolidine ring: (*S*) configuration at C12, (*R*) configuration at C17, and (*S*) configuration at C16, to which *p*-tolyl group is connected. The pyrrolidine ring has an envelope conformation with the flap atom being the C15 atom which lies  $0.280(5)$  Å out of the plane of the remaining four atoms.

The piperidine ring adopts a half-chair conformation with the phenyl-methylidene function attached to C29 and the C26 atom lying  $0.348(4)$  Å out of the plane of the remaining five atoms. The sum of the angles around the piperidine-N4 atom is approximately  $340^\circ$ , confirming its  $sp^3$  character. For the morpholinyl ring

(O3/C2/C1/N1/C4/C3), a chair conformation is apparent with O3 and N1 deviating by 0.63 and 0.68 Å respectively out of the plane of the remaining four atoms.

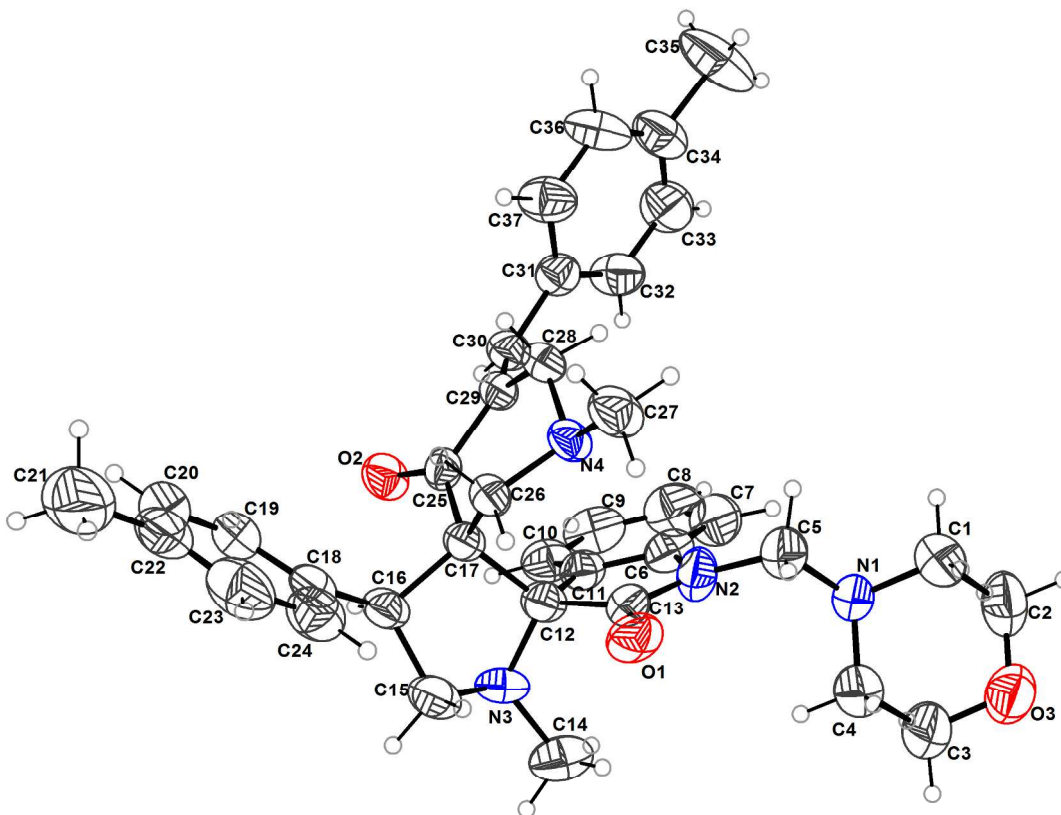


**Figure 2.** An ORTEP view of compound **7** with the atom-numbering scheme. The displacement ellipsoids are drawn at the 50% probability level and H atoms are shown as small spheres.

The two *p*-tolyl rings in **7**, (C(18)/C(19)/C(20)/C(22)/C(23)/C(24) and C(31)/C(32)/C(33)/C(34)/C(36)/C(37), are nearly planar with maximum deviation of 0.016(5) Å for atom C18 and 0.023(5) Å for atom C34. The weighted average ring bond distance in these two *p*-tolyl rings are 1.42(2) and 1.41(2) Å. The indole ring system is planar with maximum deviation of 0.066(4) Å for atom C12.

As to the crystal structure, centrosymmetric eight-membered {...HNCO}<sub>2</sub> amide dimers are the most significant features of the crystal packing. A perspective view of the crystal packing in the unit cell of compound **7** is shown in Figure 3. In the crystal

structure of **7**, molecules are linked together by an intermolecular N—H $\cdots$ O hydrogen-bonding network (Table 1). The crystal structure of **7** seems to be further stabilized by an intermolecular C—H $\cdots$  $\pi$  ( $\pi$ -ring) stacking interaction (C14—H142 $\cdots$ Cg1, where Cg1 refers to the ring centre of gravity for the 5-membered ring N2/C6 /C11/C12 /C13).

**Table 1.** Hydrogen-bond parameters ( $\text{\AA}$ ,  $^\circ$ ) of compound **7**.

$D-H\cdots A$	$D-H$	$H\cdots A$	$D\cdots A$	$D-H\cdots A$
C14—H142 $\cdots$ Cg1	0.97(2)	2.83(3)	2.92(5)	85.6(17)

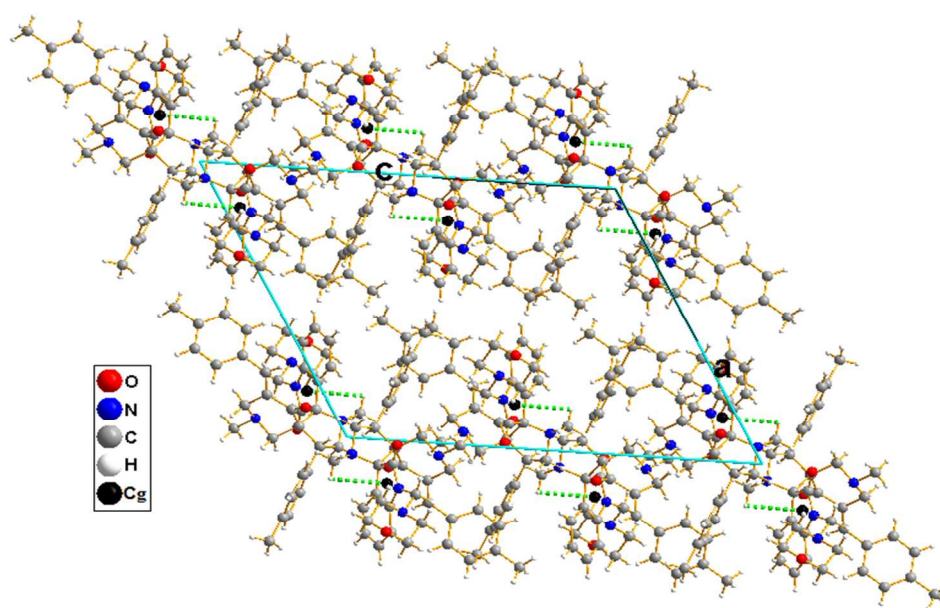


**Figure 3.** Crystal packing in the unit cell of compound **7**, showing the Cg...H $\pi$  interactions as dashed lines.

### AM1, PM3 and DFT studies

Theoretical calculations using both AM1 and PM3 methods were undertaken to compare the geometrical parameters of compound **7** obtained from the single crystal X-ray analysis with the calculated data. The geometry of **7** was optimized by the molecular mechanics force field (MM<sup>+</sup>), followed by either semi-empirical AM1 or PM3 methods implemented in the HyperChem 8.0 package. The structure was fully optimized without constraining any parameters, thus bringing all geometric variables to their equilibrium values. The energy minimization protocol employed the Polake-Ribiere conjugated

gradient algorithm. Convergence to a local minimum was achieved when the energy gradient was  $\leq 0.01$  kcal mol<sup>-1</sup>. The RHF (Restricted Hartree-Fock) method was used in the spin pairing for the two semi-empirical tools<sup>24</sup> (Figures S6, S7 of the supplementary material exhibit the optimized structure of compound **7** by AM1 and PM3 methods, respectively). Additionally, the molecular structure of **7** in the ground state (*in vacuo*) was optimized using density functional theory (DFT). In DFT energy of the molecule is determined from the electron density instead of a wave function, and this computational method has emerged as an important quantum chemical tool for studying various chemical problems.<sup>29</sup> The DFT calculations were carried out with a hybrid functional B3LYP [Becke's three parameter hybrid functional using the Lee-Young-Parr (LYP) correlation functional]<sup>30,31</sup> and 3-21G\* basis set, utilizing the Gaussian 03 package. The geometries were optimized by minimizing energies with respect to all the geometrical parameters without imposing any molecular symmetry constraints (Figure S8).

### Optimized structures

The computational chemistry studies in the present work aimed to determine geometric parameters of the optimized structures for compound **7**, and to compare them with the experimental X-ray data. Tables S1 and S2 in the supplementary material list the experimentally determined (single crystal X-ray analysis) and theoretically calculated parameters (bond lengths and angles) utilizing the AM1, PM3, and DFT methods. It is apparent, that for most of the bond lengths and angles calculated parameters from the optimized structures are close to those experimentally determined. The observed differences can be attributed to the fact that, the experimental results refer to the solid phase while those from the theoretical calculations, to the gas phase. In solid state, the existence of a crystal field and intermolecular interactions between the molecules, are the main source for the differences between the calculated and experimental data.<sup>32</sup> The maximum difference in value between experimental and calculated bond lengths using AM1, PM3, and DFT methods for compound **7** are 0.088, 0.083, and 0.067 Å, respectively, and the corresponding root mean square errors (RMSE) are 0.032, 0.033, and 0.031. It seems that all these computation methods provide good approximations of bond lengths to the experimentally obtained values.

Regarding the bond angles, the maximum difference between the experimental and calculated values for compound **7** are 6.5, 6.0, and 7.6° and the RMSE are 2.49, 2.30, and 2.33 for AM1, PM3 and DFT methods, respectively. A global comparison was performed by superimposing the molecular skeletons obtained from X-ray diffraction of compound **7** with those generated by AM1, PM3 and DFT methods (Figure 4). One can notice that most of the functions are almost aligned with each other with the exception of the morpholinyl ring attached to C5. In the theoretical optimized structures (AM1, PM3 and DFT) for compound **7**, this fragment pointing almost in opposite direction to that of the X-ray structure, as it is apparent from the values of the torsion angle C4-N1-C5-N2: AM1 (68.49°), PM3 (60.03°), and DFT (66.63°), and from X-ray data (-72.81°). This, most likely, can be attributed to the effect of crystal lattice affecting conformation of **7** in solid state, *versus* gas phase that is used in AM1, PM3, or DFT calculation methods.<sup>24,32</sup>

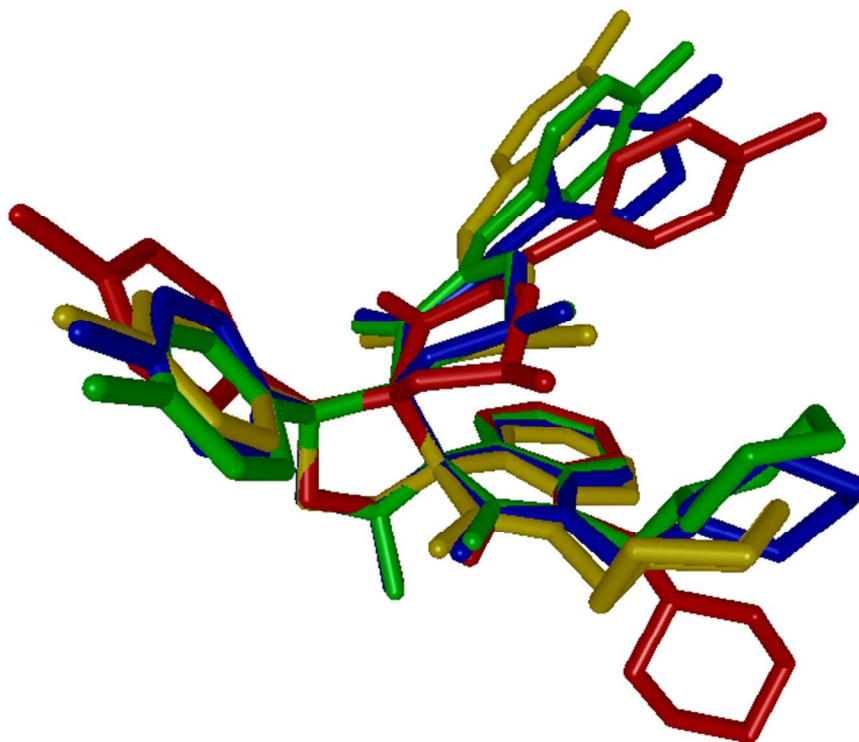


**Figure 4.** Overlay diagram of compound **7** with the central pyrrolidine rings overlapped: red (X-ray structure), green (AM1), blue (PM3) and golden yellow (DFT).

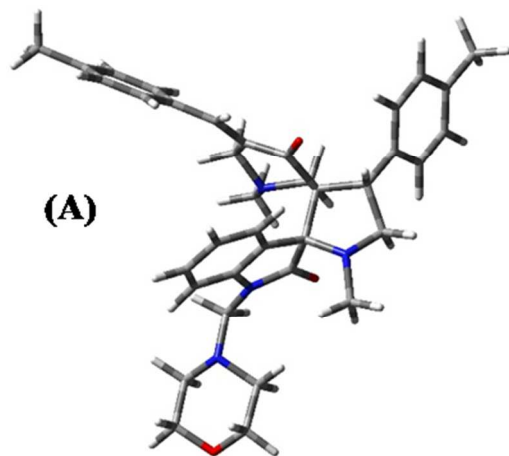
Eight different stereoisomeric forms may be observed due to cycloaddition reaction mentioned in the present study (structures **A-H**, Figure 5). Computational chemistry calculations were undertaken towards the eight hypothesized stereoisomers. This may explain the parameters governing formation of one stereoisomer among the others based on quantum chemical calculations. All calculations were performed using Gaussian 03 software. The full geometrical optimization of all stereochemical structures and transition states (TSs) were carried out with density functional theory (DFT) using nonlocal B3LYP hybrid functional and 6-31G(d,p) basis set. All geometrical optimizations were performed without symmetry constraints. Minimum energy geometries were confirmed by observing positive frequencies from the vibrational frequency calculations. Transition states obtained were confirmed by having only imaginary frequency with corresponding eigenvector involving the formation of the newly created C–C bonds. The thermal correction to the internal energy and Gibbs free energy were obtained from the vibrational frequency calculations. Figure 5 exhibits the theoretically expected 8 stereoisomers due to 3 chiral centers of compound **7** and their energy values due to Gaussian optimization [DFT/B3LYP method with 6-31G(d,p) basis set]. From the results obtained, it is obvious that stereoisomeric structure **A** reveals energy value lower than any other isomer (**B-H**). Energy values correlation observed and the experimentally stereochemical structure of **7** exhibited by X-ray studied (Figure 2) are well matched with each other supporting the phenomenon towards stereoselectivity of the conducted reaction beside the ability of utilization of quantum chemical calculation for prediction of the stereochemical structure for the stereoselective reactions.

The [3+2]-dipolar regioselective cycloaddition reaction may takes place *via* *exo*- or *endo*-trig pathway. Only one stereochemical structure was observed due to the conducted cycloaddition reaction, which structure was supported by X-ray studies (compound **7**, Figure 2). Gaussian calculations exhibits that the stereochemical structure of **7** is consistent with the *exo*-TS. In other words, the *endo*-TS is not overlapped in this stereoselective reaction. Reaction energy profile and calculation of the Gibbs energy, internal energy and the respective relative energies for the hypothesized reaction pathways support the *exo*-trig pathway. The optimized geometries of the two possible

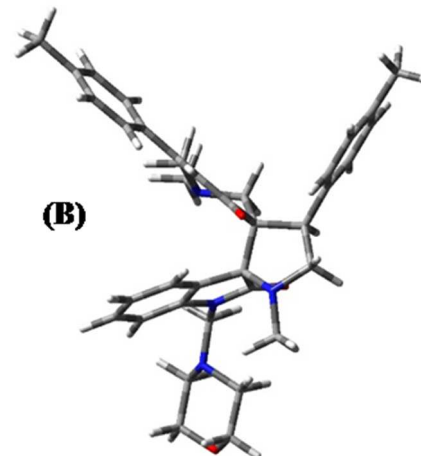
transition states derived from *exo*- and *endo*-trig pathways are shown in Figure 6. From observed data (Table 2) it is obvious that the change in internal energy favors the reaction pathway towards the *exo*-product by means of exothermic nature (-24.82 Kcal/mol) relative to the *endo*-pathway (-17.89 Kcal/mol). The activation barrier for the *endo*-stereoisomer is 44.89 Kcal/mol whereas, for the *exo*-stereoisomer is 29.02 Kcal/mol (Figure 7). These observed data are in good agreement with the experimentally stereochemical structure **7** selectivity produced by the conducted [3+2]-dipolar cycloaddition reaction. *Exo*-trig reaction allows the reaction to take place through the less hindered face giving rise to the observed stereoisomeric form of **7**.

**Table 2.** Calculated change in internal energy  $\Delta E$ , reaction Gibbs free energies  $\Delta G$ , activation Gibbs free energies  $\Delta G^\ddagger$  at theB3LYP/6-31G(d,p) “all energies are in Kcal/mol”.

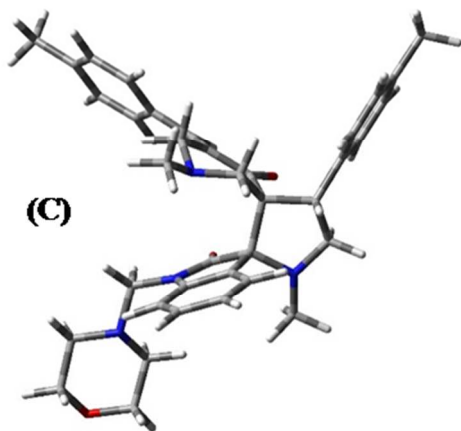
Structure	$\Delta E(\text{Kcal/mol})$	$\Delta G$	$\Delta G^\ddagger$
<i>endo</i> - trig reaction	-17.89	-1.61	44.89
<i>exo</i> -trig reaction	-24.82	-9.52	29.02



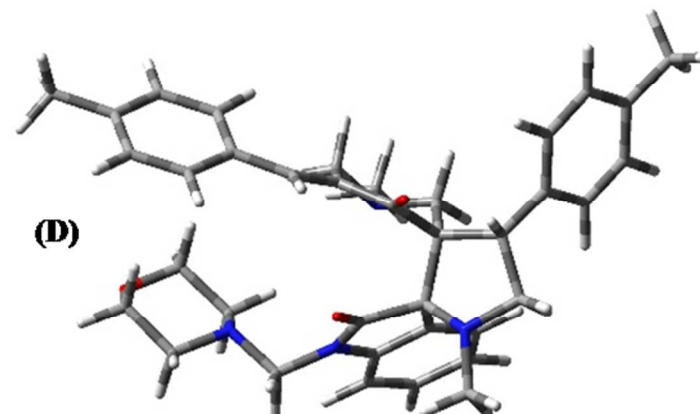
E = -1179682.26 Kcal/mol



E = -1179680.63 Kcal/mol



E = -1179676.08 Kcal/mol



E = -1179673.48 Kcal/mol

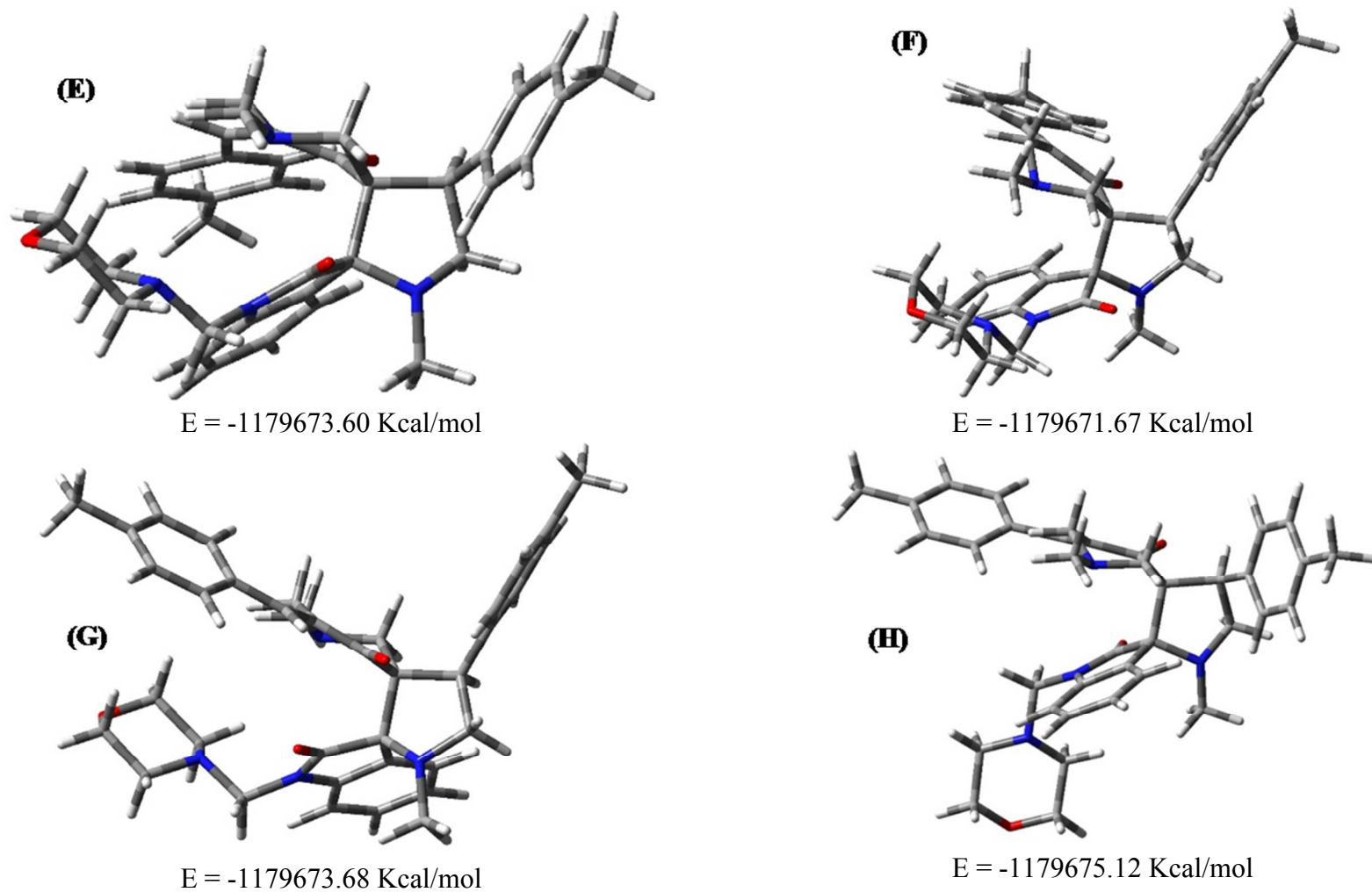


**Figure 5.** Stereoisomeric forms expected theoretically due to cycloaddition reaction and their energy values optimized by Gaussian optimization [DFT/B3LYP method with 6-31G(d,p) basis set].

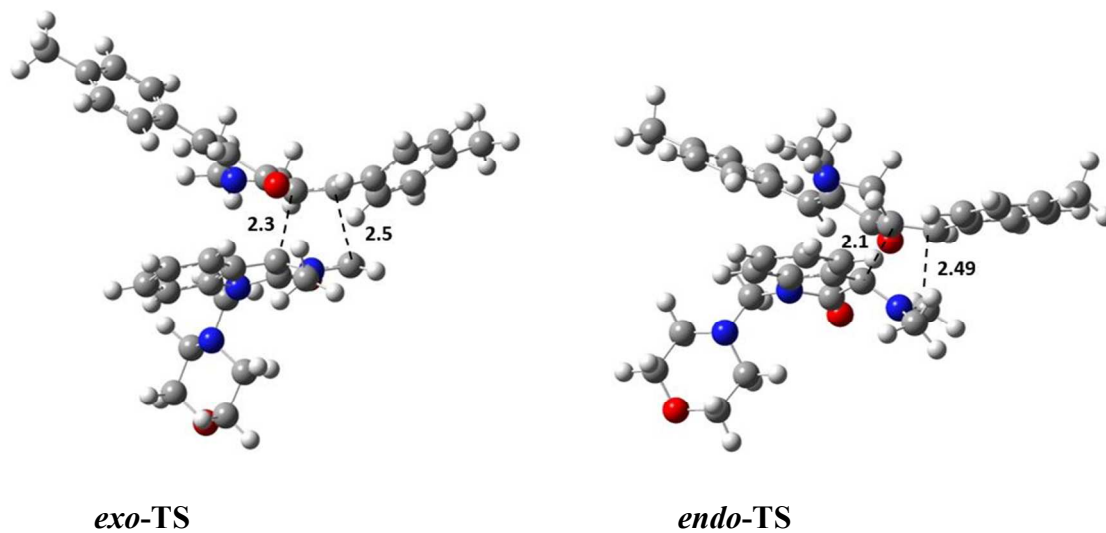


**Figure 6.** Transition state structures at the B3LYP/6-31G(d,p) corresponding to the stereoisomeric path of the cycloaddition reaction.

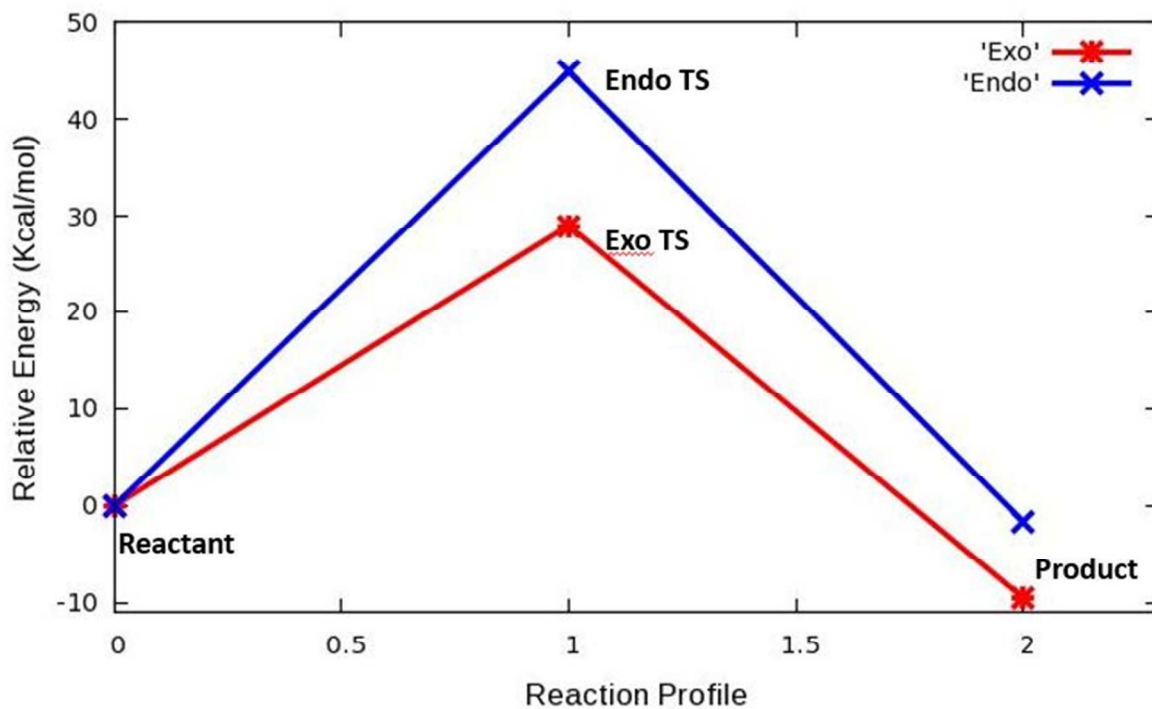


**Figure 7.** Relative energies (Kcal/mol) for the reactants, TSs and products for the *exo*- and *endo*-stereoisomeric pathways.

### Molecular electrostatic potential (MEP)

MEP is a very useful property for analyzing and predicting molecular reaction behavior. It is a good guide in assessing molecular reactivity towards positively or negatively charged reactants as well as hydrogen bonding interactions. MEP surfaces depict the size, shape and variation of electron density and correlates with dipole moment, electronegativity, partial charges and the sites of chemical reactivity within the molecule. The electrostatic potential is also well suited for analyzing processes based on the recognition of one molecule by another, as in drug-receptor, and enzyme-substrate interactions.<sup>33</sup> MEP for compound **7** was calculated using B3LYP/6-31G(d,p). The resulting overall MEP (Figure 8) exhibits that the intense (negative) red color around the carbonyl group of the piperidone ring is the most nucleophilic site. This may represent, e.g., the most favored path for approaching an electrophilic group of an enzyme/receptor, while regions with positive MEP may specify potential hydrogen bond donors for such interactions.

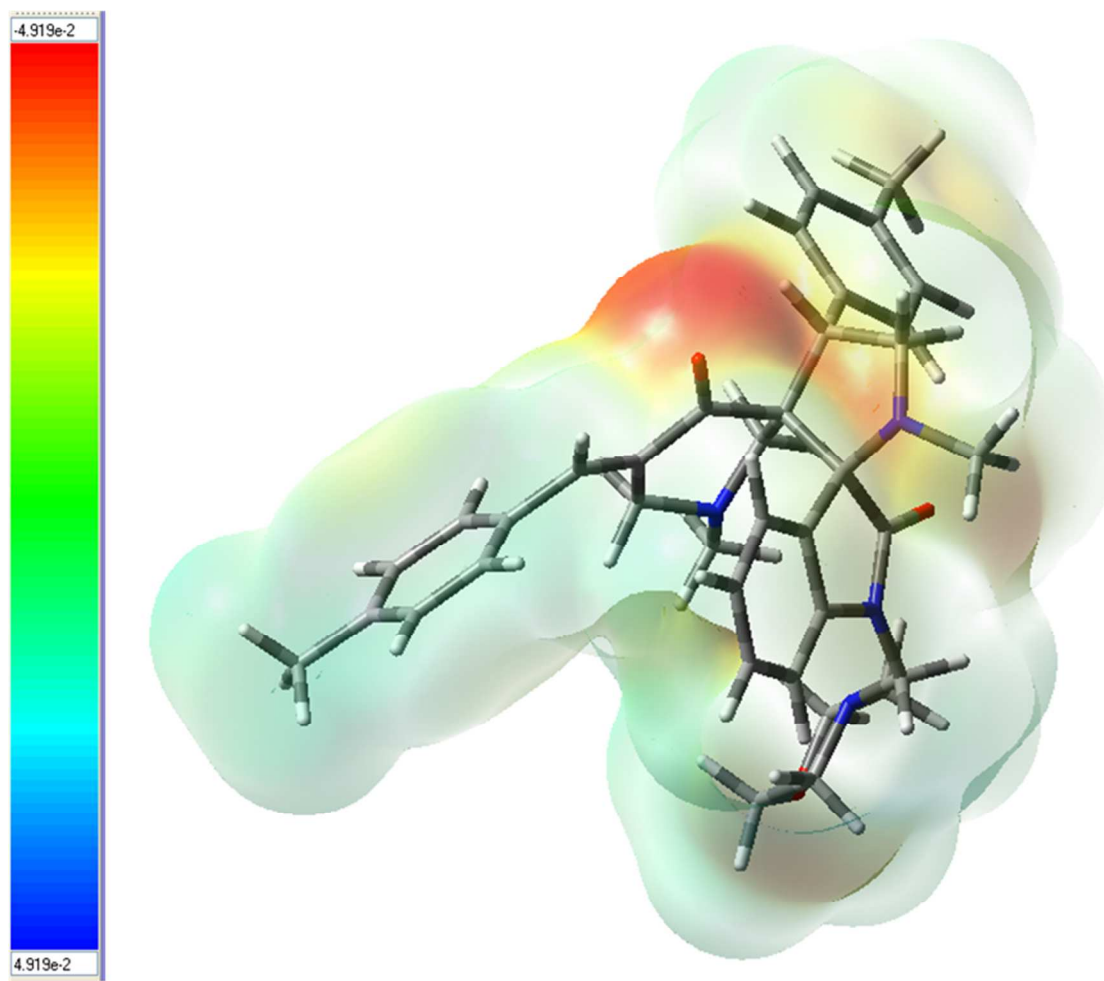


**Figure 8.** Molecular Electrostatic Potential map (MEP) of compound **7** calculated at the B3LYP/6-31G(d,p) level (in a.u.).

### Frontier molecular orbitals (FMOs)

FMOs play an important role in determining electric and optical properties, electron transition, and chemical reactivity of a compound. A LUMO (lowest unoccupied molecular orbital) is an empty molecular orbital with the ability to accept an electron, while HOMO (highest occupied molecular orbital) is an occupied molecular orbital from which electrons can be donated. For compound **7** FMOs were calculated utilizing the Gaussian 03 program package at the B3LYP/6-31G(d,p) level of theory. The results are shown in Figures 9, and 10 together with the corresponding energy levels. The indole ring in **7** mainly contributes to the HOMO molecular orbital, while the (4-methylphenyl)methylidene residue together with the piperidinyll carbonyl scaffold contribute to the LUMO. The internal energy difference between the HOMO (-0.198 eV) and LUMO (-0.066 eV) in compound **7** is 0.132 eV. The HOMO-LUMO energy gap explains the fact that intramolecular charge transfer interaction is taking place within the molecule. Low HOMO–LUMO energy gap implies low molecular stability in the sense of its high reactivity in chemical reactions. The energy gap between HOMO and LUMO indicates also high kinetic stability, high excitation energies for many of the excited states, and large chemical hardness of the molecule in terms of its nucleophilicity and electrophilicity.<sup>24</sup>

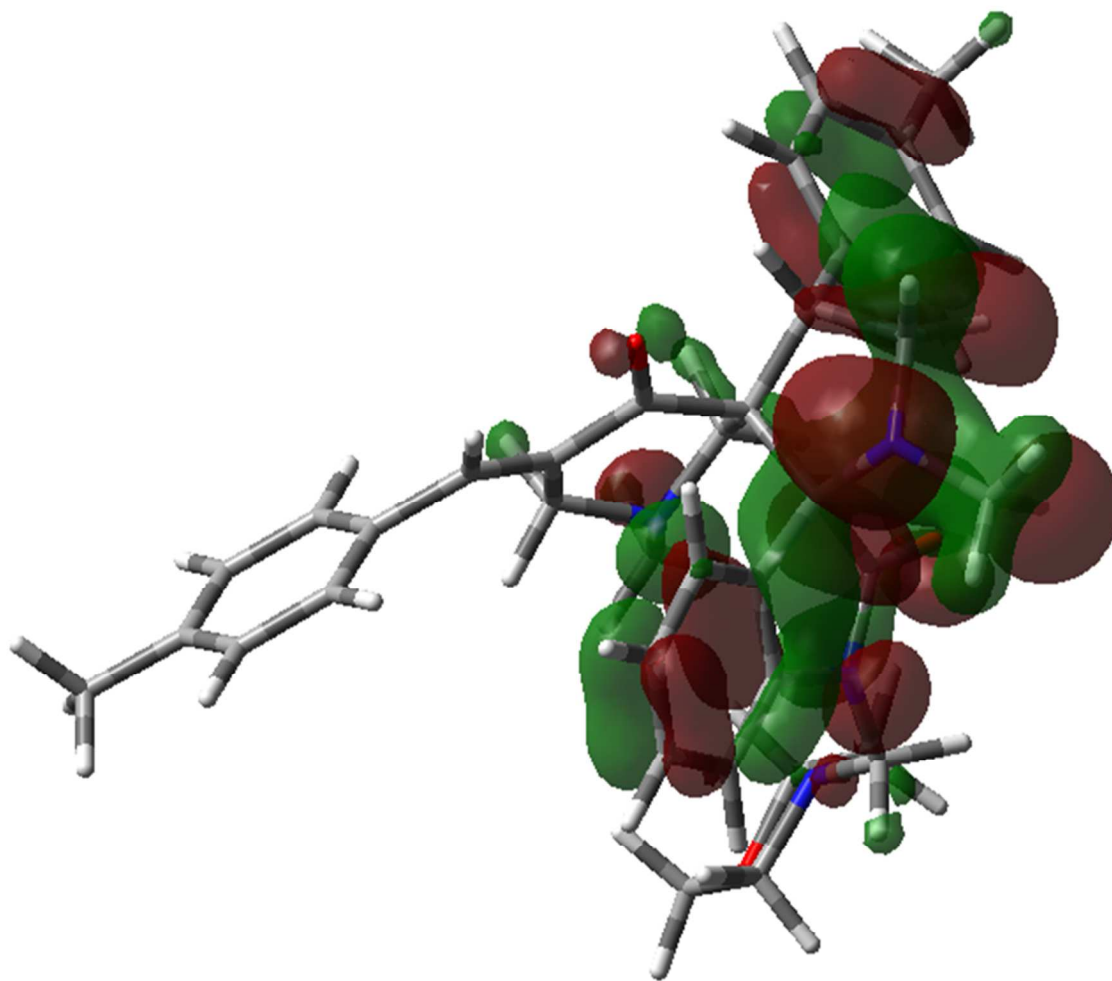


**Figure 9.** Molecular orbital surfaces of energy level (-0.198 eV) for the HOMO of compound 7 computed by the B3LYP/6-31G(d,p) method.

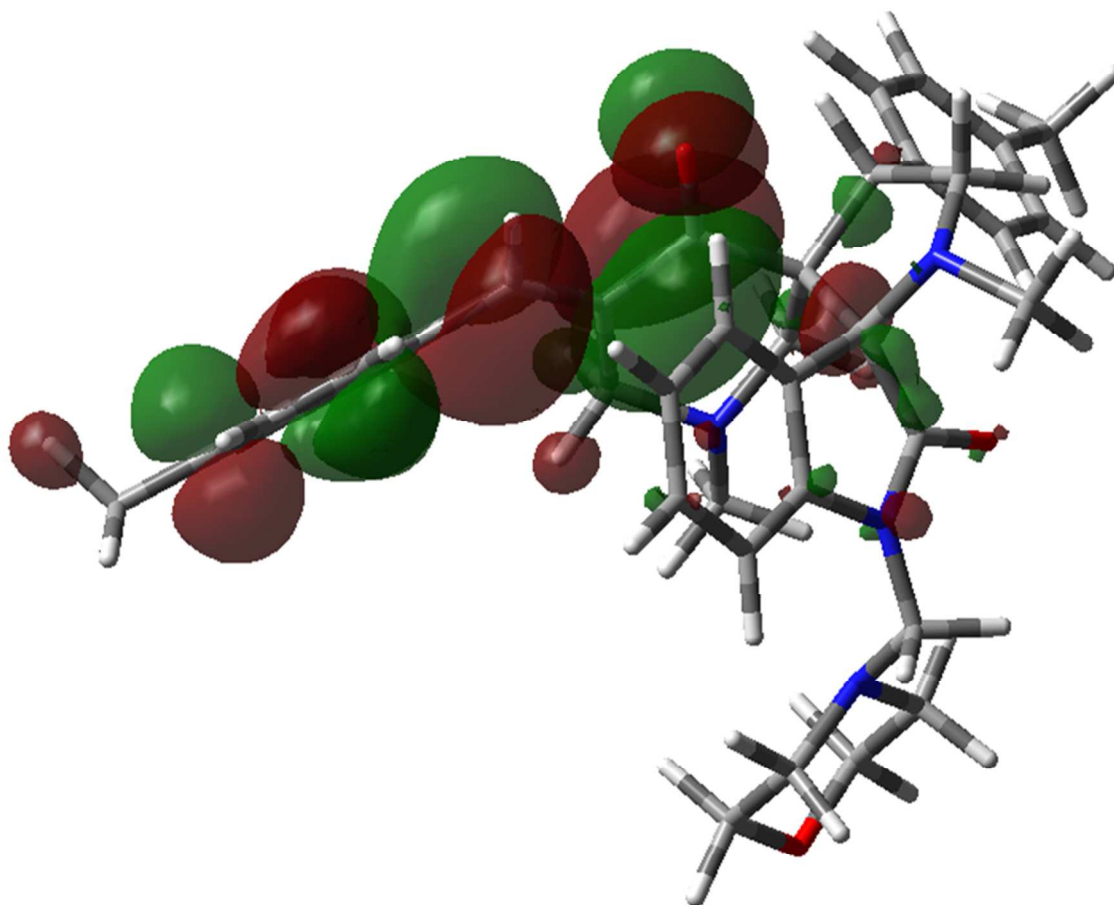


**Figure 10.** Molecular orbital surfaces of energy level (-0.066 eV) for the LUMO of compound **7** computed by the B3LYP/6-31G(d,p) method.

### Antitumor properties

The antitumor properties of spiropyrrolidine-oxindole **7** were screened against diverse human tumor cell lines representing leukemia, melanoma, and cancers of the lung, colon, brain, ovary, breast, prostate, and kidney utilizing the *in-vitro* Sulfo-Rhodamine-B (SRB) standard method.<sup>15-22,34,35</sup> From the results obtained [Table 3, Figures S9 of the supplementary material exhibits the dose response curves of compound **7** against various human tumor cell lines and Figure S10 of the supplementary material reveals the GI<sub>50</sub> “concentration resulting in a 50% growth inhibition of the tumor cell line compared with the control experiments”, TGI “concentration resulting in a total growth inhibition (100%) of the tumor cell line compared with the control experiments”, and LC<sub>50</sub> “concentration resulting in a 50% lethal of the tumor cell line compared with the control

experiment” in  $\log_{10}$  values], it appears that compound **7** possesses promising antitumor properties against most of the tested tumor cell lines. The highest potency was observed against PC-3 (prostate cancer), and HOP-92 (non-small cell lung cancer) cell lines with  $IC_{50}$  (concentration resulting in a 50% growth inhibition of the tumor cell line compared to the control experiments) = 0.831 and 1.40  $\mu\text{M}$ , respectively. Also, considerable antitumor properties were observed against A498, and UO-31 (renal cancer) cell lines ( $IC_{50}$  = 1.77  $\mu\text{M}$ ). It has also been noticed that the synthesized spiro-oxindole reveals specific antitumor inhibition selectivity against some of the tested cell lines as exhibited in prostate cancer cell lines PC-3 and DU-145 ( $IC_{50}$  = 0.831, 13.4  $\mu\text{M}$ , respectively). Table 4 shows the median growth inhibitory concentrations ( $IC_{50}$ ,  $\mu\text{M}$ ) of *in vitro* subpanel tumor cell lines of compound **7**. The lowest median growth inhibitory concentration value was observed against renal cancer cell lines (3.71  $\mu\text{M}$ ), followed by breast and non-small cell lung cancers (median growth inhibitory concentrations 4.22 and 4.23  $\mu\text{M}$ , respectively). Appreciable median growth inhibitory concentration of compound **7** was also observed for the leukemia cell line (4.36  $\mu\text{M}$ ).

**Table 3.** Antitumor screening data of compound **7** expressed as  $IC_{50}$  ( $\mu\text{M}$ ) utilizing human tumor cell lines through *in-vitro* SRB screening bio-assay.

Panel/Cell lines	$IC_{50}^*$ ( $\mu\text{M}$ )
<u>Leukemia</u>	
CCRF-CEM	5.82
K-562	3.47
MOLT-4	4.97
RPMI-8226	3.57
SR	3.97
<u>Non-Small Cell Lung Cancer</u>	
A549/ATCC	3.59
HOP-62	>100
HOP-92	1.40
NCI-H226	2.77
NCI-H23	5.74

NCI-H322M	>100
NCI-H460	5.47
NCI-H522	6.42
<u>Colon Cancer</u>	
COLO 205	8.13
HCC-2998	74.5
HCT-116	3.09
HCT-15	3.95
HT29	4.67
KM12	5.41
SW-620	4.62
<u>CNS Cancer</u>	
SF-268	4.83
SF-295	4.21
SF-539	17.2
SNB-19	9.61
SNB-75	2.30
U251	4.43
<u>Melanoma</u>	
LOX IMVI	12.8
MALME-3M	5.79
M14	4.88
MDA-MB-435	4.59
SK-MEL-2	8.59
SK-MEL-28	32.6
SK-MEL-5	3.54
UACC-257	4.89
UACC-62	5.58
<u>Ovarian Cancer</u>	
IGROV1	96.4
OVCAR-4	2.76

OVCAR-5	>100
OVCAR-8	4.50
NCI/ADR-RES	5.63
SK-OV-3	>100
<u>Renal Cancer</u>	
786-0	6.73
A498	1.77
ACHN	3.62
CAKI-1	2.90
SN12C	5.44
TK-10	>100
UO-31	1.77
<u>Prostate Cancer</u>	
PC-3	0.831
DU-145	13.4
<u>Breast Cancer</u>	
MCF7	3.00
MDA-MB-231/ATCC	4.71
HS 578T	5.16
BT-549	7.19
T-47D	3.15
MDA-MB-468	2.12

\*IC<sub>50</sub> is the concentration resulting in a 50% growth inhibition of the tumor cell line compared with the control experiments.

**Table 4.** Median growth inhibitory concentrations (IC<sub>50</sub>, μM) of *in vitro* subpanel tumor cell lines of compound 7.

Panel	Median growth inhibitory concentrations (IC <sub>50</sub> , μM)
Leukemia	4.36
Non-Small Cell Lung Cancer	4.23
Colon Cancer	14.91

CNS Cancer	7.10
Melanoma	9.25
Ovarian Cancer	27.32
Renal Cancer	3.71
Prostate Cancer	7.12
Breast Cancer	4.22
Full panel IC <sub>50</sub> ( $\mu$ M) meangraph- midpoint (MG-MID)	9.14

### Conclusion

1',1''-Dimethyl-4'-(4-methylphenyl)-5''-[(4-methylphenyl)methylidene]-1-[(4-morpholinyl)methylene]-dispiro[3*H*-indole-3,2'-pyrrolidine-3',3''-piperidine]-2(1*H*),4''-dione (**7**) was synthesized regioselectively through a 1,3-dipolar cycloaddition reaction of non-stabilized azomethine ylide, (generated *in situ* via a decarboxylative condensation of 1-[(4-morpholinyl)methylene]-1*H*-indole-2,3-dione **4** with sarcosine **5**) and 3*E*,5*E*-bis[(4-methylphenyl)methylidene]-1-methyl-4-piperidone **6**. Single crystal X-ray analysis of spiropyrrolidine-oxindole **7** provided support the structural assignment and permitted determination of configurations of three chiral centers preset in this molecule. The calculated bond lengths and angles for compound **7** utilizing the AM1, PM3, and DFT methods were in good agreement with those experimentally determined by X-ray analysis. Gaussian calculations exhibits that the stereochemical structure of **7** is consistent with the *exo*-TS. *Exo*-trig reaction allows the reaction to take place through the less hindered face giving rise to the observed stereoisomeric form of **7**. The molecular electrostatic potential (MEP) of **7** [calculated by DFT, B3LYP/6-31G(d,p) level of theory] delineated the carbonyl group of the piperidone ring is the most nucleophilic site. The frontier molecular orbitals (FMOs) calculations for compound **7** revealed that the indole ring contributes mainly to the HOMO (-0.198 eV), while the (4-methylphenyl)methylidene scaffold together with the piperidinyl carbonyl group contribute to the LUMO (-0.066 eV), with the energy gap difference of 0.132 eV. Compound **7** exhibits promising antitumor properties against diverse tumor cell lines representing leukemia, melanoma and cancers of the lung, colon, brain, ovary, breast,

prostate, and kidney in the Sulfo-Rhodamine-B standard bio-assay. A remarkable potency of **7** observed against PC-3 (prostate cancer), HOP-92 (non-small cell lung cancer), A498, and UO-31 (renal cancer) cell lines.

## Experimental

### Materials and methods

Melting points were recorded in open capillary tubes on a digital Stuart SMP3 melting point apparatus. The IR spectra (KBr) were recorded on a JASCO 6100 FT-IR spectrophotometer. <sup>1</sup>H-nuclear magnetic resonance (<sup>1</sup>H-NMR), <sup>13</sup>C-NMR, <sup>1</sup>H,<sup>1</sup>H-COSY and HSQC spectra were recorded on a Bruker Ascend 400/R (<sup>1</sup>H: 400, <sup>13</sup>C:100 MHz) spectrometer. The starting materials **4**<sup>36</sup> and **6**<sup>37</sup> were prepared according to the previously reported procedures.

Synthesis of 1',1''-dimethyl-4'-(4-methylphenyl)-5''-[(4-methylphenyl)methylidene]-1-[(4-morpholinyl)methylene]-dispiro[3*H*-indole-3,2'-pyrrolidine-3',3''-piperidine]-2(1*H*),4''-dione (**7**)

A mixture of equimolar amounts of 3*E*,5*E*-bis[(4-methylphenyl)methylidene]-1-methyl-4-piperidone (**6**) (5 mmol), 1-[(4-morpholinyl)methylene]-1*H*-indole-2,3-dione (**4**) and sarcosine (**5**) in absolute ethanol (25 mL) was refluxed for 12 h. The reaction mixture was concentrated to half of its initial volume and left at room temperature overnight. The separated solid was collected and crystallized from ethanol affording **7** as colorless microcrystals, m.p. 198-200 °C, yield 75% (2.21 g). IR (in KBr)  $\nu$  (cm<sup>-1</sup>): 1703, 1686, 1609, 1512. <sup>1</sup>H-NMR (CDCl<sub>3</sub>)  $\delta$  (ppm): 1.62 (d, *J* = 12.80 Hz, 1H, upfield H of piperidinyl *H*<sub>2</sub>*C*-2''), 1.98 (s, 3H, piperidinyl NCH<sub>3</sub>), 2.12 (s, 3H, pyrrolidinyl NCH<sub>3</sub>), 2.29 (s, 3H, ArCH<sub>3</sub>), 2.30 (s, 3H, ArCH<sub>3</sub>), 2.54 (t, *J* = 4.58 Hz, 4H, morpholinyl 2NCH<sub>2</sub>), 2.84 (dd, *J* = 2.60, 14.48 Hz, 1H, upfield H of piperidinyl *H*<sub>2</sub>*C*-6''), 3.23-3.30 (m, 3H, downfield H's of piperidinyl *H*<sub>2</sub>*C*-2'', *H*<sub>2</sub>*C*-6'' and upfield H of pyrrolidinyl *H*<sub>2</sub>*C*-5'), 3.62 (t, *J* = 4.58 Hz, 4H, morpholinyl 2OCH<sub>2</sub>), 3.90 (dd, *J* = 8.78, 11.22 Hz, 1H, downfield H of pyrrolidinyl *H*<sub>2</sub>*C*-5'), 4.07 (d, *J* = 12.52 Hz, 1H, upfield H of NCH<sub>2</sub>N), 4.50 (d, *J* = 12.52 Hz, 1H, downfield H of NCH<sub>2</sub>N), 4.78 (dd, *J* = 6.98, 11.26 Hz, 1H, pyrrolidinyl HC-4'), 6.75 (d, *J* = 8.00 Hz, 1H, arom. H), 6.87 (d, *J* = 8.00 Hz, 2H, arom. H), 6.96-7.26

(m, 10H, 9 arom. H + olefinic CH).  $^{13}\text{C}$ -NMR ( $\text{CDCl}_3$ )  $\delta$  (ppm): 21.1 ( $\text{ArCH}_3$ ), 21.4 ( $\text{ArCH}_3$ ), 35.0 (pyrrolidinyl  $\text{NCH}_3$ ), 45.0 (piperidinyl  $\text{NCH}_3$ ), 45.1 (pyrrolidinyl  $\text{HC-4}'$ ), 51.2 (morpholinyl  $\text{NH}_2\text{C-3/5}$ ), 56.7 (piperidinyl  $\text{H}_2\text{C-6}''$ ), 57.3 (pyrrolidinyl  $\text{H}_2\text{C-5}'$  + piperidinyl  $\text{H}_2\text{C-2}''$ ), 62.5 ( $\text{NCH}_2\text{N}$ ), 66.3 [spiro  $\text{C-3}'$  ( $\text{C-3}''$ )], 66.8 (morpholinyl  $\text{OH}_2\text{C-2/6}$ ), 75.5 [spiro  $\text{C-3}$  ( $\text{C-2}'$ )], 108.7, 122.1, 126.7, 127.4, 128.7, 128.9, 129.2, 130.0, 132.4, 132.6, 135.2, 136.3, 137.6, 138.9, 144.5 (arom.  $\text{C}$  + olefinic  $\text{CH}$ ), 176.4 [oxindolyl  $\text{C=O}$  ( $\text{C-2}$ )], 198.4 [piperidinyl  $\text{C=O}$  ( $\text{C-4}''$ )]. Elemental analysis:  $\text{C}_{37}\text{H}_{42}\text{N}_4\text{O}_3$  required C, 75.23; H, 7.17; N, 9.48. found C, 75.30; H, 7.26; N, 9.61.

### Single crystal X-ray studies

A colorless single crystal of **7** has been selected and mounted onto thin glass fibers. X-Ray single crystal diffraction data were collected at room temperature (298 K) on an Enraf-Nonius 590 diffractometer with a Kappa CCD detector using graphite monochromated  $\text{Mo-K}\alpha$  ( $\lambda = 0.71073 \text{ \AA}$ ) radiation. Reflection data has been recorded in the rotation mode using the  $\phi$  and  $\omega$  scan technique with  $2\theta_{\text{max}} = 27.49$  and  $27.45$ . In the absence of significant anomalous scattering, Friedel pairs have been merged. Changes in illuminated volume were kept to a minimum, and were taken into account by the multi-scan inter-frame scaling.<sup>38</sup> Unit cell parameters were determined from least-squares refinement with  $\theta$  in the range  $0 \leq \theta \leq 27$  and  $3 \leq \theta \leq 27$ . The structure of **7** was solved by direct methods using *SUPERFLIP*<sup>39</sup> implemented in *CRYSTALS* program suit.<sup>40</sup> The refinement was carried out by full-matrix least-squares method on the positional and anisotropic temperature parameters of all non-hydrogen atoms based on  $F^2$  using *CRYSTALS* package.<sup>40</sup> All hydrogen atoms were positioned geometrically and were initially refined with soft restraints on the bond lengths and angles to regularize their geometry ( $\text{C-H}$  in the range 0.93–0.98) and  $U_{\text{iso}}(\text{H})$  (in the range 1.2–1.5 times  $U_{\text{eq}}$  of the parent atom). Then, the positions were refined with riding constraints.<sup>41</sup> The general-purpose crystallographic tool *PLATON*<sup>42</sup> was used for the structure analysis and presentation of the results. The molecular graphics were done using *ORTEP-3* for Windows<sup>43</sup> and *DIAMOND*<sup>44</sup> programs. Details of the data collection conditions and the parameters of the refinement process are given in Table 5.

**Table 5.** Crystal data and structure refinement parameters of compound 7.

Crystal data	Compound 7
CCDC deposition no.	1037056
Chemical formula	C <sub>37</sub> H <sub>42</sub> N <sub>4</sub> O <sub>3</sub>
$M_r$	590.77
Crystal system, space group	Monoclinic, $P2_1/c$
Temperature (K)	298
$a, b, c$ (Å)	16.6007 (10), 11.3683 (10), 20.5655 (10)
$\beta$ (°)	120
$V$ (Å <sup>3</sup> )	3361.18 (16)
$Z$	4
Radiation type	Mo $K\alpha$
$\mu$ (mm <sup>-1</sup> )	0.08
Crystal size (mm)	0.49 × 0.23 × 0.12
$\Delta\rho_{\max}, \Delta\rho_{\min}$ (e Å <sup>-3</sup> )	0.24, -0.34
$(\sin \theta/\lambda)_{\max}$ (Å <sup>-1</sup> )	0.657
Data, restraints, parameters	2915, 187, 259
$R[F^2 > 2\sigma(F^2)], wR(F^2), S$	0.048, 0.098, 0.97

**Antitumor activity bio-assay**

Screening for antitumor activity of compound 7 against 56 different human tumor cell lines, including leukemia, melanoma, and cancers of the lung, colon, brain, ovary, breast, prostate and kidney, was carried out according to the *in-vitro* Sulfo-Rhodamine-B (SRB) standard method<sup>15-22,34,35</sup> by US-National Cancer Institute (Bethesda, Maryland, USA). The human tumor cell lines of the cancer screening panel were grown in RPMI-1640 medium containing 5% fetal bovine serum and 2 mM L-glutamine. For a typical screening experiment, cells were inoculated in 96-well-microtiter plates in 100  $\mu$ L at plating densities ranging from 5000 to 40,000 cells/well depending on the doubling time of individual cell lines. After cell inoculation, the microtiter plates were incubated at 37 °C, 5% CO<sub>2</sub>, 95% air and 100% relative humidity for 24 h prior to addition of the test compound. After 24 h, two plates of each cell lines were fixed in situ with trichloroacetic

acid (TCA), to represent a measurement of the cell population for each cell line at the time of test compound addition (time zero,  $T_z$ ). The tested compound was solubilized in dimethylsulfoxide at 400-fold the desired final maximum test concentration and stored frozen prior to use. At the time of the test compound addition, an aliquot of frozen concentrate was thawed and diluted to twice the desired final maximum test concentration with a complete medium containing 50  $\mu\text{g}/\text{mL}$  gentamicin. Aliquots of 100  $\mu\text{L}$  of the tested compound dilutions were added to the appropriate microtiter wells already containing 100  $\mu\text{L}$  of medium, to give in the required final concentrations. Following the test compound addition, the plates were incubated for additional 48 h at 37  $^{\circ}\text{C}$ , 5%  $\text{CO}_2$ , 95% air and 100% relative humidity. For adherent cells, the assay was terminated by the addition of cold TCA. Cells were fixed in situ by the gentle addition of 50  $\mu\text{L}$  of cold 50% (w/v) TCA (final concentration, 10% TCA) and incubated for 60 min at 4  $^{\circ}\text{C}$ . The supernatant was discarded, and the plates were washed five times with tap water and air dried. Sulforhodamine B (SRB) solution (100  $\mu\text{L}$ ) at 0.4% (w/v) in 1% acetic acid was added to each well, and the plates were incubated for 10 min at room temperature. After staining, unbound dye was removed by washing five times with 1% acetic acid and the plates were air dried. Bound stain was subsequently solubilized with 10 mM trizma base, and the absorbance was read on an automated plate at 515 nm. For suspension cells, the methodology was the same except that the assay was terminated by fixing settled cells at the bottom of the wells by gently adding 50  $\mu\text{L}$  of 80% TCA (final concentration, 16% TCA). The activity was screened at serial dilutions ( $10^{-4}$ – $10^{-8}$   $\mu\text{M}$ ). Using the seven absorbance measurements [time zero ( $T_z$ ), control growth ( $C$ ) and test growth in the presence of the tested compound at the five concentration levels ( $T_i$ )], the percentage growth was calculated at each of the tested compound concentration levels.

Percentage growth inhibition was calculated as  $[(T_i - T_z)/(C - T_z)] \times 100$  for concentrations in which  $T_i \geq T_z$ , and by  $[(T_i - T_z)/T_z] \times 100$  for concentrations for which  $T_i < T_z$ .

Growth inhibition of 50% ( $IC_{50}$ ) was calculated from  $[(Ti-Tz)/(C-Tz)] \times 100 = 50$ , which is the test compound concentration resulting in a 50% reduction in the net protein increase (as measured by SRB staining) in control cells during the drug incubation (Tables 3, and 4).

### Acknowledgment

This study was supported financially by the Science and Technology Development Fund (STDF), Egypt, Grant No. 1357.

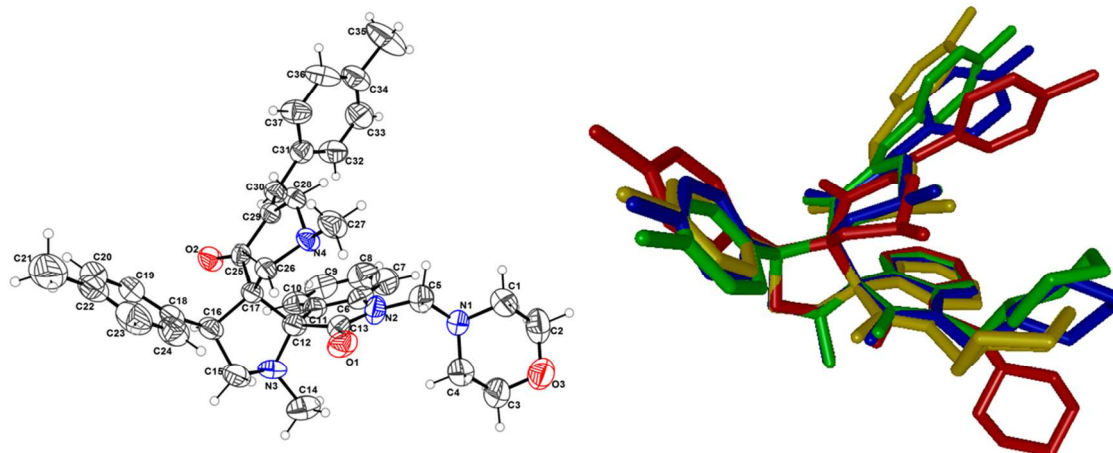
### Notes and references

- 1 H. Frankish, *Lancet*, 2003, **361**, 1278.
- 2 D. Belpomme, P. Irigaray, A. J. Sasco, J. A. Newby, V. Howard, R. Clapp and L. Hardell, *Int. J. Oncol.*, 2007, **30**, 1037–1049.
- 3 T. Helleday, E. Petermann, C. Lundin, B. Hodgson and R.A. Sharma, *Nat. Rev. Cancer*, 2008, **8**, 193–204.
- 4 C. Are, S. Rajaram, M. Are, H. Raj, B. O. Anderson, R. C. Swamy, M. Vijayakumar, T. Song, M. Pandey, J. A. Edney and E. L. Cazap, *Journal of Surgical Oncology*, 2013, **107**, 221–226.
- 5 E. Carrasco, P. J. Álvarez, C. Melguizo, J. Prados, E. Álvarez-Manzaneda R. Chahboun, I. Messouri, M. I. Vázquez-Vázquez, A. Aránega and F. Rodríguez-Serrano, *Eur. J. Med. Chem.*, 2014, **79**, 1–12.
- 6 L. W. Zheng, Y. Li, D. Ge, B. X. Zhao, Y. R. Liu, H. S. Lv, J. Ding and J. Y. Miao, *Bioorg. Med. Chem. Lett.*, 2010, **20**, 4766–4770.
- 7 L. Zhang, Q. Zheng, Y. Yang, H. Zhou, X. Gong, S. Zhao and C. Fan, *Eur. J. Med. Chem.*, 2014, **82**, 139–151.
- 8 S. Faivre, G. Demetri, W. Sargent and E. Raymond, *Nat. Rev. Drug Discov.*, 2007, **6**, 734–745.
- 9 T. J. Abrams, L. B. Lee, L. J. Murray, N. K. Pryer and J. M. Cherrington, *Mol. Cancer Ther.*, 2003, **2**, 471–478.
- 10 D. B. Mendel, A. D. Laird, X. Xin, S. G. Louie, J. G. Christensen, G. Li, R. E. Schreck, T. J. Abrams, T. J. Ngai, L. B. Lee, L. J. Murray, J. Carver, E. Chan, K.

- G. Moss, J. O. Haznedar, J. Sukbuntherng, R. A. Blake, L. Sun, C. Tang, T. Miller, S. Shirazian, G. McMahon and J. M. Cherrington, *Clin. Cancer Res.*, 2003, **9**, 327–337.
- 11 H. Prenen, J. Cools, N. Mentens, C. Folens, R. Sciote, P. Schoffski, A. Van Oosterom, P. Marynen and M. Debiec-Rychter, *Clin. Cancer Res.* 2006, **12**, 2622–2627.
- 12 E. Garcia Prado, M. D. Garcia Gimenez, R. De la Puerta Vázquez, J.L. Espartero Sánchez and M. T. Sáenz Rodriguez, *Phytomedicine*, 2007, **14**, 280–284.
- 13 C. B. Cui, H. Kakeya and H. Osada, *Tetrahedron*, 1996, **52**, 12651–12666.
- 14 C. B. Cui, H. Kakeya and H. Osada, *J. Antibiot.*, 1996, **49**, 832–835.
- 15 A. S. Girgis, S. S. Panda, M. N. Aziz, P. J. Steel, C. D. Hall and A. R. Katritzky, *RSC Advances*, 2015, **5**, 28554–28569.
- 16 A. S. Girgis, S. S. Panda, E. M. Shalaby, A. F. Mabied, P. J. Steel, C. D. Hall and A. R. Katritzky, *RSC Advances*, 2015, **5**, 14780–14787.
- 17 A. S. Girgis, S. S. Panda, I. S. Ahmed Farag, A. M. El-Shabiny, A. M. Moustafa, N. S. M. Ismail, G. G. Pillai, C. S. Panda, C. D. Hall and A. R. Katritzky, *Org. Biomol. Chem.*, 2015, **13**, 1741–1753.
- 18 R. F. George, N. S. M. Ismail, J. Stawinski and A. S. Girgis, *Eur. J. Med. Chem.*, 2013, **68**, 339–351.
- 19 A. M. Moustafa, A. S. Girgis, S. M. Shalaby and E. R. T. Tiekink, *Acta Crystallogr., Sect. E: Struct. Rep. Online*, 2012, **E68**, o2197–o2198.
- 20 A. S. Girgis, J. Stawinski, N. S. M. Ismail and H. Farag, *Eur. J. Med. Chem.*, 2012, **47**, 312–322.
- 21 A. S. Girgis, *Eur. J. Med. Chem.*, 2009, **44**, 1257–1264.
- 22 A. S. Girgis, *Eur. J. Med. Chem.*, 2009, **44**, 91–100.
- 23 H. D. Flack and G. Bernardinelli, *Chirality*, 2008, **20**, 681–690.
- 24 E. M. Shalaby, A. S. Girgis, A. M. Moustafa, A. M. ElShaabiny, B. E. M. El-Gendy, A. F. Mabied and I. S. Ahmed Farag, *J. Mol. Structure*, 2014, **1075**, 327–334.
- 25 I. S. Ahmed Farag, A. S. Girgis, A. A. Ramadan, A. M. Moustafa and A. F. Mabied, *Acta Crystallogr., Sect. E: Struct. Rep. Online*, 2014, **E70**, o379–o380.

- 26 I. S. Ahmed Farag, A. S. Girgis, A. A. Ramadan, A. M. Moustafaa and E. R. T. Tiekink, *Acta Crystallogr., Sect. E: Struct. Rep. Online*, 2014, **E70**, o70–o71.
- 27 I. S. Ahmed Farag, A. S. Girgis, A. A. Ramadan, A. M. Moustafaa and E. R. T. Tiekink, *Acta Crystallogr., Sect. E: Struct. Rep. Online*, 2014, **E70**, o43–o44.
- 28 I. S. Ahmed Farag, A. S. Girgis, A. A. Ramadan, A. M. Moustafaa and E. R. T. Tiekink, *Acta Crystallogr., Sect. E: Struct. Rep. Online*, 2014, **E70**, o22–o23.
- 29 P. Rawat and R. N. Singh, *J. Mol. Structure*, 2014, **1074**, 201–212.
- 30 A. D. Becke, *J. Chem. Phys.*, 1993, **98**, 5648–5652.
- 31 C. Lee, W. Yang and R. G. Parr, *Phys. Rev. B*, 1988, **37**, 785–789.
- 32 E. İnkaya, M. Dinçer, Ö Ekici and A. Cukurovali, *Spectrochim. Acta Mol. Biomol. Spectros. Part A*, 2013, **101**, 218–227.
- 33 L. A. Taib, H. M. Faidallah, Z. S. Şahin, A. M. Asiri, O. Şahin and M. N. Arshad, *J. Mol. Structure*, 2014, **1076**, 272–279.
- 34 A. R. Katritzky, A. S. Girgis, S. Slavov, S. R. Tala and I. Stoyanova-Slavova, *Eur. J. Med. Chem.*, 2010, **45**, 5183–5199.
- 35 A. S. Girgis, H. M. Hosni and F. F. Barsoum, *Bioorg. Med. Chem.*, 2006, **14**, 4466–4476.
- 36 V. R. Solomon, C. Hu and H. Lee, *Bioorg. Med. Chem.*, 2009, **17**, 7585–7592.
- 37 H. I. El-Subbagh, S. M. Abu-Zaid, M. A. Mahran, F. A. Badria and A. M. Al-Obaid, *J. Med. Chem.*, 2000, **43**, 2915–2921.
- 38 C. H. Görbitz, *Acta Cryst. B*, 1999, **55**, 1090–1098.
- 39 L. Palatinus and G. Chapuis, *J. Appl. Cryst.*, 2007, **40**, 786–790.
- 40 P. W. Betteridge, J. R. Carruthers, R. I. Cooper, K. Prout and D. J. Watkin, *J. Appl. Cryst.*, 2003, **36**, 1487.
- 41 R. I. Cooper, A. L. Thompson and D. J. Watkin, *J. Appl. Cryst.*, 2010, **43**, 1100–1107.
- 42 A. L. Spek, *Acta Crystallogr. D*, 2009, **65**, 148–155.
- 43 L. J. Farrugia, *J. Appl. Cryst.*, 2012, **45**, 849–854.
- 44 K. Brandenburg, DIAMOND. Crystal Impact GbR, Bonn, Germany, 2012.

## Graphical abstract



DFT studies of an anti-proliferative active spiro-oxindole against diverse tumor cell lines were reported.